Journal of
Materials Chemistry A

ROYAL SOCIETY
OF CHEMISTRY

PAPER

View Article Online
View Journal

Cite this: DOI: 10.1039/d5ta03299g

Biodegradable starch-based hydrogel as a multifunctional SEI for ultra-stable and flexible zinc-ion batteries†

Zinan Wang,[a] Tianxu Ji,[a] Qilin Zhang,[a] Peng Wang, *[abc] Xiaoyu Yang,[a] Shuo Zhang,[a] Yuhang Jin,[a] Xiaolong Fan,[a] Jiaxuan Zhang,[a] Wei Duan,[ab] Ying Yue,[ab] Yang Ju[d] and Yunpeng Liu[e]

Received 26th April 2025
Accepted 7th July 2025

DOI: 10.1039/d5ta03299g

rsc.li/materials-a

Constructing an artificial solid electrolyte interface (SEI) layer is an effective strategy to suppress dendrite growth and corrosion in aqueous zinc batteries (AZBs). However, 2D material-based SEI coatings are generally non-biodegradable, posing environmental risks due to their persistence in soil. This research introduces a starch/polyacrylamide (STA/PAAm) hydrogel membrane developed as a self-healing SEI layer for AZBs. The incorporation of biomass-derived starch endows the STA/PAAm hydrogel with excellent soil biodegradability, achieving complete degradation within 21 days. Meanwhile, its dual-network structure, reinforced by reversible Al^{3+} crosslinking, offers robust mechanical resilience, self-healing ability, and high ionic conductivity—presenting a sustainable alternative to conventional SEI materials. Theoretical calculations reveal that the hydrogel modulates Zn^{2+} solvation, forming a stable $[Zn(H_2O)_4(STA)(AAm)]^{2+}$ configuration, which suppresses hydrogen evolution and promotes uniform Zn^{2+} deposition along the (002) plane. The STA/PAAm-coated Zn anode exhibits an extended lifespan of over 3000 h at 2 mA cm^{-2}, significantly surpassing that of bare Zn (531 h). Paired with an AlVO-NMP cathode, the pouch-type full cell retains 87.2% capacity after 2000 cycles at 5 A g^{-1} and demonstrates remarkable flexibility, powering LEDs under bending and folding conditions. This work bridges high-performance energy storage with environmental sustainability, offering a green paradigm for flexible batteries.

Introduction

In recent years, aqueous zinc-ion batteries (AZBs) have gained significant attention for energy storage applications due to their high safety, cost-effectiveness, environmental compatibility, and robust electrochemical performance.[1–4] Despite these advantages, the Zn anode, a key component of AZBs, encounters critical challenges, including dendrite formation, corrosion, and undesired side reactions.[5–7] These issues severely limit cycle life, stability, energy efficiency, and operational safety of AZBs.[8,9] Consequently, it is crucial to enhance the surface structure of the Zn anode and optimize its interaction with the electrolyte to suppress dendrite formation, corrosion, and side reactions to achieve improved performance of AZBs.

The development of an artificial solid electrolyte interface (SEI) layer on the Zn anode surface has emerged as a promising solution to these challenges.[10–12] Conventional surface modification approaches for Zn anodes utilize coatings such as graphene,[13] metal–organic frameworks (MOFs),[14–17] carbon nanotubes (CNTs),[18,19] and Mxene,[20–22] which represent advanced 2D materials. These inorganic coatings offer excellent electrical conductivity and chemical stability, which significantly enhance the electrochemical performance of Zn anodes. However, these materials also present challenges, including high production costs and complex fabrication processes. While many of these materials are designed to be durable, concerns have arisen regarding their long-term environmental impact, particularly their potential persistence and degradation in natural environments. Recent research has focused on improving the degradability and recyclability of these materials, but achieving a balance between performance and environmental sustainability remains a complex issue.[23]

Hydrogel electrolytes, owing to their exceptional flexibility, ionic conductivity, and environmental friendliness, are increasingly recognized as indispensable components in flexible AZBs. Their unique three-dimensional crosslinked network

---

[a] *School of Energy, Power and Mechanical Engineering, North China Electric Power University, Baoding, 071000, China. E-mail: wang.peng.ncepu@foxmail.com*

[b] *Hebei Key Laboratory of Electric Machinery Health Maintenance & Failure Prevention, North China Electric Power University, Baoding 071003, China*

[c] *Key Laboratory of Icing and Anti/De-icing, China Aerodynamics Research and Development Center, Mianyang, Sichuan 621000, China*

[d] *School of Mechanical Engineering, Zhejiang University, Hangzhou, 310058, China*

[e] *Department of Electrical Engineering, North China Electric Power University, Baoding, 071000, China*

† Electronic supplementary information (ESI) available. See DOI: https://doi.org/10.1039/d5ta03299g

structures offer highly tunable porous pathways that effectively direct the transport of Zn^{2+} ions, significantly suppressing dendrite growth and side reactions. Moreover, the abundant hydrophilic functional groups within the hydrogel can form reversible coordination with Zn^{2+} ions, thereby enhancing the stability of the electrode–electrolyte interface and facilitating uniform Zn^{2+} deposition through favorable ion transport kinetics.[24] More importantly, hydrogels derived from natural polymers or their composite networks exhibit outstanding biodegradability and self-healing capabilities, making them ideal candidates for the development of wearable and sustainable zinc-based energy systems.[25,26] Through multiscale structural engineering, double-network or multi-network hydrogel systems integrate sacrificial bond design and cooperative energy dissipation mechanisms, achieving a balanced enhancement of mechanical toughness and electrochemical stability. This provides a solid foundation for the realization of high-strength, long-life flexible AZBs.

Biomass-based materials have garnered increasing attention in recent years due to their affordability, renewability, environmental friendliness, and distinct functional properties.[27] Among these, starch (STA), a representative biomass material, exhibits exceptional film-forming ability, biodegradability, and biocompatibility, making it a promising candidate for applications in AZBs.[28] By copolymerizing STA with acrylamide (AAm), a starch/polyacrylamide (STA/PAAm) hydrogel can be obtained. The incorporation of multivalent ions facilitates the formation of a robust double-network structure, which significantly enhances the hydrogel's adhesion, mechanical strength, self-healing capability, and ionic conductivity. These improved properties contribute to the stabilization and performance enhancement of Zn anodes. Therefore, starch-based double-network, self-healing hydrogel coatings represent a novel and sustainable strategy for interfacial modification, offering a potential solution to the key challenges associated with Zn anodes in AZBs.

In this study, a $Zn(OTf)_2$ double-network hydrogel membrane based on STA and AAm polymerization (referred to as "STA/PAAm") was developed as an SEI coating for Zn anodes. This coating demonstrates high ionic conductivity and superior mechanical properties. The incorporation of high-valence Al^{3+} into the STA/PAAm hydrogel facilitates multivalent coordination and reversible interactions between Al^{3+} and the hydrogel's functional groups, enabling rapid recovery from damage and imparting self-healing properties.[29] Furthermore, the biomass-based nature of STA allows the hydrogel to biodegrade under microbial action, breaking down into harmless small molecules or natural substances, thereby mitigating environmental pollution.[30] Density functional theory (DFT) and molecular dynamics (MD) calculations reveal that the oxygen-containing groups in STA and AAm interact strongly with Zn^{2+}, replacing surrounding water molecules and modifying its solvation structure. Within the STA/PAAm hydrogel, $Zn[(H_2O)_6]^{2+}$ transitions to a novel solvation configuration, $Zn[(H_2O)_4(STA)(AAm)]^{2+}$, which effectively suppresses hydrogen evolution reactions (HER) and interfacial corrosion. The hydrogel's network structure facilitates efficient Zn^{2+} migration pathways, promoting uniform Zn deposition. At an areal capacity of 2 mA h cm^{-2}, STA/PAAm-coated Zn anodes (STA/PAAm@Zn) achieve a stable lifespan of 3000 h, significantly surpassing the 531 h of bare Zn anodes. Additionally, the STA/PAAm@Zn//AlVO-NMP full cell exhibits excellent electrochemical performance, retaining over 87.2% of its capacity after 2000 cycles at a high current density of 5 A g^{-1}.

Materials and methods

Materials

The acrylamide (AAm, tannic acid, $Al_2(SO_4)_3\cdot 18H_2O$ (AR, 99%), V_2O_5 (AR, 99%), and $AlCl_3\cdot 6H_2O$ (AR, 97%) were obtained from Aladdin Reagent Co., Ltd, Shanghai, China. Starch (STA), zinc trifluoromethanesulfonate ($Zn(CF_3SO_3)_2$/$Zn(OTf)_2$) (AR, 99%), ammonium persulfate (AR, 99.5%), *N*-methyl-2-pyrrolidone (NMP) (AR, 99%), and *N*,*N*-methylene bisacrylamide(MBAA) were supplied by McLean Biochemical Technology Co., Ltd, Shanghai, China. Polyvinylidene fluoride (PVDF) was procured from Keroas Innovative Technology Co., Ltd, Dongguan, China. Super P was purchased from Canrd New Energy Technology Co., Ltd, Guangdong, China. Carbon cloth (CC) was purchased from Suzhou Keshenghe Metal Materials Co., Ltd, Suzhou, China. Anhydrous ethanol and H_2O_2 (30%) were obtained from Sinopharm Chemical Reagent Co., Ltd, Shanghai, China. All chemicals were used without further purification.

Synthesis of STA/PAAm@Zn

Initially, 1 g of starch (STA) was dissolved in 10 mL of water at 60 °C. Subsequently, 1 g of acrylamide (AAm), 0.1 g of tannic acid, 0.2 g of $Al_2(SO_4)_3\cdot 18H_2O$, 7.27 g of $Zn(OTf)_2$, 0.005 g of *N*,*N*-methylene bisacrylamide, and 0.005 g of ammonium persulfate were added sequentially to the STA solution. The mixture was stirred thoroughly at room temperature and poured into a mold for polymerization. The polymerization was conducted by drying the mixture in an oven at 40 °C for 6 h to produce an STA/PAAm hydrogel film. This hydrogel film was subsequently coated onto zinc foil to prepare STA/PAAm@Zn. To produce hydrogel films with different STA mass fractions, varying amounts of STA (0%, 5%, 10%, and 15% of the total mass) were dissolved in 10 mL of water at 60 °C. The resulting films were designated as STA-0%/PAAm, STA-5%/PAAm, STA-10%/PAAm, and STA-15%/PAAm, respectively.

Preparation of AlVO-NMP electrode

According to a reported method, $Al_xV_2O_5\cdot nH_2O$ was synthesized using a hydrothermal process.[31] Specifically, 0.364 g of V_2O_5 and 2 mL of 30% H_2O_2 were added to 60 mL of water under constant stirring. Once the V_2O_5 dissolved, 2.414 g of $AlCl_3\cdot 6H_2O$ was introduced into the solution. After stirring for 0.5 h, the mixture was transferred to a polytetrafluoroethylene-lined stainless steel reactor and heated at 120 °C for 5 h. The reactor was then allowed to cool naturally to room temperature, yielding $Al_xV_2O_5\cdot nH_2O$. To remove partial crystallization water, the $Al_xV_2O_5\cdot nH_2O$ sample was heated at 200 °C for 5 h in a vacuum drying oven. The resulting material was immersed in *n*-methyl-2-

pyrrolidone (NMP) and subsequently filtered. After filtration, the sample was dried at 60 °C for 10 h in a vacuum drying oven to produce AlVO-NMP. A slurry was prepared by combining AlVO-NMP, Super P, and PVDF in a 7 : 3 : 1 weight ratio, with NMP added to achieve the desired consistency. The mixture was thoroughly ground into a uniform paste and applied onto a 0.01 mm stainless steel mesh. Following drying at 60 °C for 24 h, the AlVO-NMP cathode was obtained, with an active material loading of about 1 mg cm^{-2}.

Assembled batteries

Two STA/PAAm@Zn electrodes were configured into a symmetrical cell (STA/PAAm@Zn//STA/PAAm@Zn). Additionally, a full cell (STA/PAAm@Zn//AlVO-NMP) was assembled using STA/PAAm@Zn as the anode and AlVO-NMP as the cathode. To fabricate STA/PAAm@Cu, the STA/PAAm hydrogel film was applied onto a copper foil, which was then paired with a Zn electrode to assemble a Zn//STA/PAAm@Cu asymmetric battery. In CR2032-type coin cells, 80 μL of 2 M $Zn(OTf)_2$ was used as the electrolyte, with a 0.62 mm-thick glass fiber membrane as the separator. The cathode (AlVO-NMP) was fabricated as a 6 mm diameter disk containing approximately 1.13 mg of active material (AlVO-NMP), and the anode (bare Zn or STA/PAAm@Zn) was a 7 mm diameter disk. In flexible pouch cells, the cathode (AlVO-NMP) measured 56 mm × 43 mm with an active material loading of about 24 mg, while the anode (bare Zn or STA/PAAm@Zn) measured 58 mm × 45 mm. All specific capacities were calculated based on the mass of the cathode active material (AlVO-NMP).

Electrochemical measurements

The electrochemical performance of half and full cells was evaluated at room temperature using CR-2032 button cells and pouch cells. Constant current charge–discharge (GCD) tests were performed using the Neware Battery Test System (BTS4000, Shenzhen, China). For Zn//Cu asymmetric batteries, the charging cutoff voltage was set at 0.5 V. Additional electrochemical characterizations, including Tafel analysis, chronoamperometry (CA), linear sweep voltammetry (LSV), and electrochemical impedance spectroscopy (EIS), were carried out using the CHI 760E electrochemical workstation (Shanghai Chenhua). The open circuit voltage and internal resistance of pouch cells were measured with the HK-3560 precision internal resistance tester.

Results and discussions

The design and synthesis process of STA/PAAm hydrogel is depicted in Fig. 1a and S1.† Starch (STA), derived from wheat, is dissolved in water at 60 °C to form a homogeneous solution, which constitutes the first hydrogel network layer. Subsequently, AAm is introduced and crosslinked to establish a double-network structure(STA/PAAm), enhancing the mechanical strength and flexibility of the hydrogel membrane. Scanning electron microscope (SEM) images (Fig. 1b and S2†) reveal a micron-scale porous structure within the hydrogel, resulting from strong crosslinking between STA and AAm. This porous architecture facilitates ion transport by providing pathways for Zn^{2+} migration, thereby improving electrochemical performance. Cross-sectional SEM and EDS images (Fig. S3†) further confirm that the STA/PAAm-based SEI forms a compact and uniform interfacial layer on the Zn anode surface, with an average thickness of approximately 30 μm. Gravimetric analysis shows that each hydrogel film weighs approximately 9.17 mg, corresponding to an areal density of about 5.96 mg cm^{-2}. Additionally, both STA and PAAm chains are rich in oxygen-containing functional groups such as –OH and $-CONH_2$. These groups can effectively coordinate with Zn^{2+} ions, facilitating their adsorption and desolvation at the interface, thereby accelerating Zn^{2+} transport through the hydrogel matrix. Owing to the selective binding and release of Zn^{2+} by these functional groups, the STA/PAAm hydrogel film not only serves as a stable artificial SEI coating to suppress side reactions and interfacial corrosion but also functions as a Zn^{2+}-conductive layer, achieving integrated mechanical and electrochemical performance. Moreover, to endow the hydrogel with self-healing capability, trivalent Al^{3+} ions were incorporated as dynamic crosslinking agents. These ions are uniformly distributed within the dual-network structure and form reversible coordination bonds, creating dynamic crosslinking points. This enables the hydrogel film to reconfigure its molecular chains upon damage and exhibit excellent self-healing behavior (Fig. 1c–e).

The complete XPS spectrum of STA/PAAm (Fig. 1f) shows peaks corresponding to C 1s, O 1s, S 2p, and Al 2p.[32–34] Within the O 1s region, peaks at 533.4 eV, 532.5 eV, and 531.5 eV are attributed to H–O–C, C=O, and Al–O groups, respectively (Fig. 1g).[35,36] The C=O signal originates from the $-CONH_2$ groups of AAm, while the H–O–C peak corresponds to hydroxyl groups in STA. Additionally, the Al–O peak arises from the coordination environment of Al^{3+} ions in $Al_2(SO_4)_3$. In the Al 2p region, two peaks at 74.2 eV and 75.4 eV are observed, corresponding to Al–O and Al in SO_4^{2-} coordination environments, respectively (Fig. S4†). The XPS analysis confirms the formation of hydrogen bonding between the $-CONH_2$ (C=O) groups of AAm and the H–O–C groups of STA, which connects the two network components. These hydrogen bonds provide additional crosslinking points and generate adhesive forces within the double-network structure, further enhancing the hydrogel's mechanical properties.[37] The inclusion of tannic acid improves adhesion to the Zn anode surface, ensuring robust attachment and preventing peeling or degradation during operation. This enhanced adhesion effectively protects the Zn anode and maintains the integrity of the coating, as demonstrated in Fig. S5.† (ref. 38)

The biodegradability of the STA/PAAm hydrogel membrane as an SEI coating for Zn anodes primarily depends on the synergistic interaction between its natural and synthetic polymer components (Fig. 2a).[39,40] STA, a plant-derived natural polyphenol, demonstrates excellent degradability, breaking down into harmless small molecules through the activity of soil microorganisms such as bacteria and fungi.[41] The amide groups ($-CONH_2$) in AAm enhance the hydrogel's interaction with

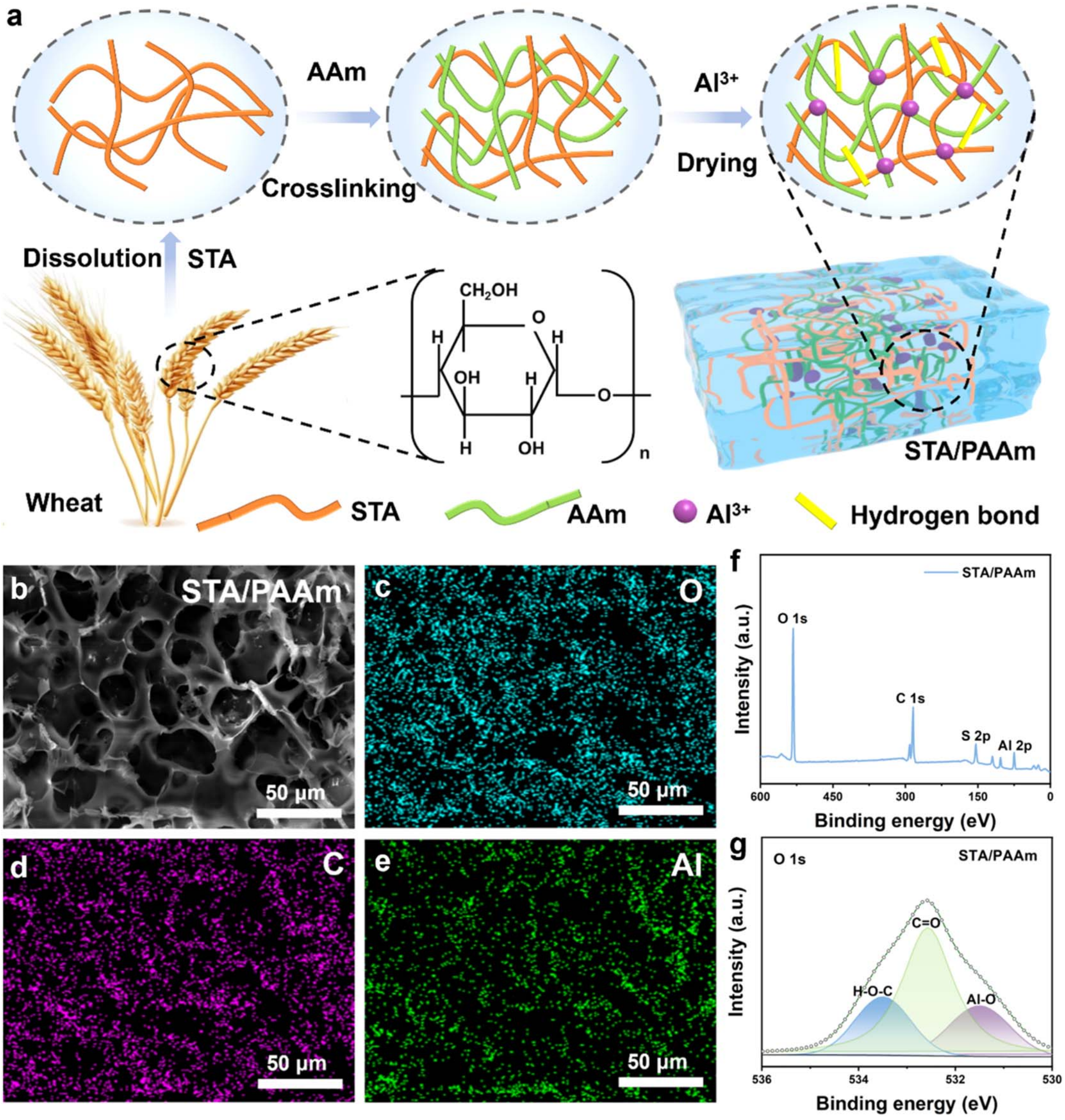

Fig. 1 (a) Schematic illustration of STA/PAAm hydrogel. (b) SEM image of STA/PAAm hydrogel. (c–e) EDS images of STA/PAAm hydrogel film. (f) Full XPS spectra of STA/PAAm hydrogel. (g) High-resolution XPS spectrum of O 1s in STA/PAAm hydrogel.

moisture and microbial enzymes, accelerating its decomposition process.[42] This dual functionality allows the STA/PAAm coating to provide effective ion transport pathways and structural stability during operation while decomposing after use, preventing environmental pollution. The resulting degradation products can be absorbed by plants, further promoting ecological recyclability. In contrast, conventional SEI materials such as MOFs, MXenes, CNTs, and graphene typically require complex synthesis routes involving high temperatures, strong acids, or organic solvents. These processes are energy-intensive and pose environmental risks, while the materials themselves are generally non-degradable under natural conditions, resulting in a high environmental burden over their life cycle (Table S1†).[43]

The extent of hydrogel degradation was largely controlled by the amount of STA incorporated (Fig. 2b). The tests were conducted in naturally air-dried yellow loam soil (pH 6.5–7.0) harboring active microbial communities under ambient conditions (22–30 °C). Residual mass was quantified through periodic sampling, soil removal, drying, and gravimetric analysis (Fig. S6 and Table S2†). Hydrogels without STA exhibited no microbial degradation after 21 days, with only a minor mass reduction attributable to water evaporation. At 5% STA content, white mold was observed on the hydrogel surface after 21 days. When STA content increased to 10%, microbial activity was substantially accelerated: white mold appeared within 7 days, accompanied by significant volume shrinkage at day 14 and complete degradation (0% residual mass) by day 21. These results demonstrate that STA incorporation plays a critical role in enhancing microbial activity and extracellular enzyme secretion, thereby accelerating the hydrogel biodegradation process.

To address the mechanical demands of SEI membranes in Zn batteries, extensive mechanical testing was conducted to

Fig. 2 (a) Schematic diagram of STA/PAAm hydrogel degradation. (b) Photographs of the biodegradation process of STA/PAAm hydrogel with varying STA mass fractions.

ensure the STA/PAAm hydrogel meets the required durability and stability.[44] The STA/PAAm hydrogel's self-healing and mechanical properties were assessed under various conditions to determine its suitability as an SEI film. Mechanical damage during battery operation, such as volume changes caused by Zn plating/stripping and the growth of Zn dendrites, imposes considerable stress on the SEI membrane.[45] Therefore, it is crucial to optimize the membrane's mechanical properties to ensure its structural integrity and long-term performance. The self-healing ability of the STA/PAAm hydrogel was preliminarily evaluated by cutting the sample into two pieces, reassembling them, and wrapping them in cling film to allow healing over a period of three days. Post-healing, the hydrogel demonstrated sufficient strength to lift a 5 g weight with ease (Fig. S7†). Upon mechanical damage, portions of the crosslinked network are disrupted. However, the dynamic crosslinking nodes provided by Al^{3+} ions within the hydrogel facilitate the reconstruction of the broken chains. As a high-valent ion, Al^{3+} forms robust ionic crosslinks that are stronger than those formed by monovalent or lower-valent ions. These ions can simultaneously form coordination bonds with multiple negatively charged functional groups, such as the –OH groups in STA and the O atoms in the –$CONH_2$ groups of AAm (Fig. 3a).[46] This ability to form multiple dynamic crosslinks enables the hydrogel network to reconnect and restore its structure after mechanical failure or deformation.

Notably, Al^{3+} coordination may locally compete with covalent crosslinkers such as MBAA, potentially affecting the stability of the primary hydrogel network. To examine this effect, we fixed the STA-to-AAm mass ratio and systematically varied the Al^{3+} precursor concentration ($Al_2(SO_4)_3 \cdot 18H_2O$), followed by tensile tests before and after healing (Fig. S8†). The results indicate that when 0.2 g of $Al_2(SO_4)_3 \cdot 18H_2O$ is added per 10 mL of water, the hydrogel exhibits optimal mechanical performance: an initial elongation at break of 579%, maintaining 545% after the first healing cycle, and retaining ~73% of its original performance even after six cut-heal cycles (Fig. 3b). These results confirm that, within an appropriate concentration range, the introduction of Al^{3+} not only preserves the primary network structure but also significantly enhances the hydrogel's mechanical resilience and repeated healing capability *via* dynamic crosslinking. In contrast, excessive Al^{3+} disrupts the network, resulting in deteriorated mechanical performance, indicating the necessity for concentration optimization. These findings demonstrate that STA/PAAm hydrogel effectively regulates interfacial stress during battery cycling, mitigating dendrite-induced structural damage and improving SEI mechanical robustness. More importantly, its self-healing

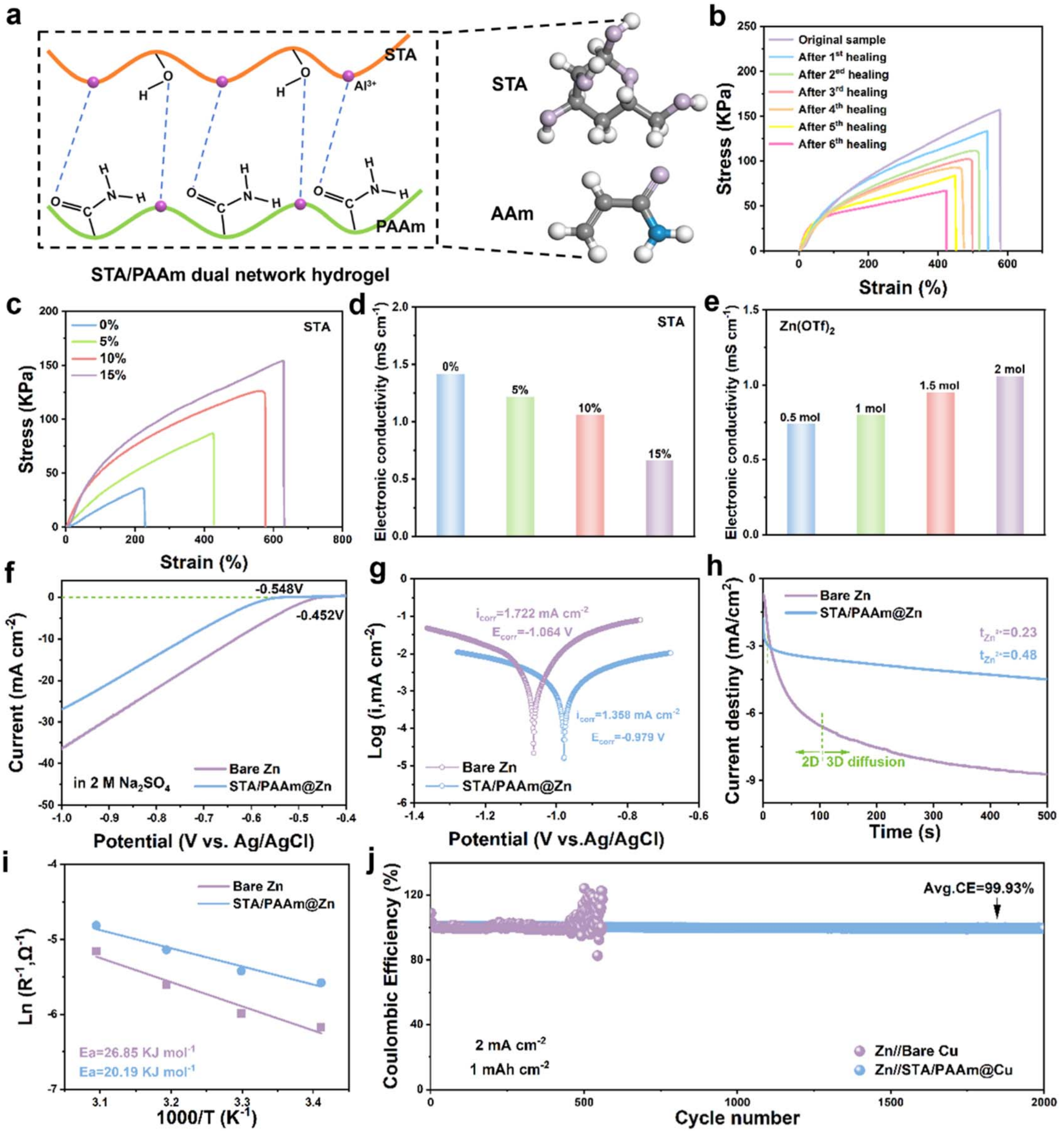

Fig. 3 (a) Structure of STA and PAAm monomer (AAm), and the mutual coupling diagram of Al^{3+} attached to a double-network molecular chain. (b) Tensile property tests of STA/PAAm hydrogel (with an addition of $Al_2(SO_4)_3\cdot18H_2O$ of 0.2 g/10 mL water after different shear self-healing times. (c) Tensile testing of STA/PAAm hydrogel films with varying mass fractions of STA. (d) Effect of STA mass fraction on the ionic conductivity of STA/PAAm. (e) Ionic conductivity of STA/PAAm at different concentrations of $Zn(OTf)_2$. (f) LSV curves for bare Zn and STA/PAAm@Zn in a 2 M Na_2SO_4 aqueous solution at 5 mV s^{-1}. (g) Tafel plots of corrosion behaviors for bare Zn and STA/PAAm@Zn in a 2 M $Zn(OTf)_2$ electrolyte. (h) Chronoamperograms at a −150 mV overpotential. (i) Arrhenius curves and (j) coulombic efficiency (CE) for Zn plating/stripping on bare Cu and STA/PAAm@Cu measured at a current density of 2 mA cm^{-2} with a capacity of 1 mA h cm^{-2}.

ability not only restores mechanical continuity but also plays a crucial role in maintaining long-term electrochemical stability. During repeated Zn^{2+} plating/stripping, conventional SEI films tend to develop microcracks or delamination. However, the dynamic network structure of STA/PAAm hydrogel enables autonomous repair of such defects, preserving ionic conductivity pathways and suppressing dendrite propagation. Unlike brittle, irreversibly damaged SEI films, the viscoelastic and regenerative nature of STA/PAAm hydrogel allows it to accommodate volume fluctuations and recover structurally in real time. This dynamic healing mechanism helps prevent localized mechanical damage from escalating into catastrophic interface failure, thereby significantly enhancing the cycle life and interfacial stability of the Zn anode.

The mechanical and electrochemical properties of STA/PAAm hydrogel membranes with varying STA mass fractions were further assessed through tensile and conductivity tests. Results indicated that STA content had a substantial impact on both tensile strength and elongation (Fig. 3c and S9–S11†). As STA content increased, the tensile strength and elongation improved, highlighting STA's role as a critical crosslinking agent and reinforcing component within the hydrogel's molecular network. AAm also contributed to the hydrogel's stretchability as its content increased (Fig. S12†). Among the tested formulations, the STA-10%/PAAm hydrogel achieved the best performance, with a tensile strength of 126.28 kPa and an elongation of about 580%, demonstrating superior elasticity and ductility. However, when STA content increased to 15%, the tensile strength increased modestly to 630%, but the rate of improvement slowed considerably. This effect is likely due to excessive crosslinking at higher STA levels, which reduces molecular flexibility and limits the material's ductility under high strain. Over-crosslinking can lead to increased brittleness, reducing the hydrogel's adaptability in dynamic mechanical environments. In contrast, STA content had a negative effect on the hydrogel's ionic conductivity (Fig. 3d and S13†). While the STA-10%/PAAm hydrogel demonstrated excellent ionic conductivity of 1.06 mS cm^{-1}, a further increase in STA content to 15% caused conductivity to drop significantly to 0.66 mS cm^{-1}. Higher STA content increases the crosslinking density of the hydrogel network, reducing the availability of free water and limiting the space for electrolyte ion movement. This constrains the formation of effective ion conduction pathways, thereby hindering ionic conductivity. While increased STA content enhances mechanical strength, it significantly decreases ionic conductivity, adversely impacting electrochemical performance. Based on these observations, a STA content of 10% is identified as the optimal ratio for STA/PAAm hydrogel membranes, offering a balance between superior stretchability and adequate ionic conductivity. In this study, Zn(OTf)$_2$ was incorporated as a doping ion source during the preparation of the STA/PAAm hydrogel. As illustrated in Fig. 3e and S14,† increasing the Zn(OTf)$_2$ concentration markedly improved the hydrogel's ionic conductivity. Zn(OTf)$_2$ provides mobile Zn^{2+} ions that traverse the gel network under an electric field, thereby enhancing ion conduction. When the Zn(OTf)$_2$ concentration in the STA/PAAm hydrogel reached 2 mol, the ionic conductivity of STA-10%/PAAm was about 1.06 S cm^{-1}. For subsequent experiments, the STA/PAAm hydrogel membrane with 10% STA content and 2 mol Zn(OTf)$_2$ concentration (designated as STA/PAAm) was selected as the primary test sample due to its optimal combination of mechanical and electrochemical properties.

The corrosion-resistant performance of the STA/PAAm coating in the electrolyte was evaluated using a three-electrode system, with bare Zn and STA/PAAm@Zn as working electrodes, Pt foil as the counter electrode, and Ag/AgCl as the reference electrode. Linear sweep voltammetry (LSV) was conducted in 2 M Na_2SO_4 aqueous solution at a scan rate of 5 mV s^{-1} to analyze the coating's effect on suppressing the HER. As shown in Fig. 3f, the HER overpotential of the STA/PAAm@Zn electrode was −0.548 V, more negative than the −0.452 V observed for bare Zn. This indicates that the STA/PAAm coating effectively suppresses the decomposition of H_2O and the generation of H_2. The higher binding energies of STA-H_2O and AAm-H_2O compared to H_2O–H_2O suggest that water molecules preferentially interact with the oxygen-containing groups of STA and AAm, disrupting the intrinsic hydrogen bond network of H_2O–H_2O and reducing the activity of free H_2O molecules (Fig. S15†).[47,48] The Tafel polarization curve further demonstrates the coating's corrosion resistance, with the corrosion current density of STA/PAAm@Zn measured at 1.358 mA cm^{-2}, significantly lower than the 1.722 mA cm^{-2} of bare Zn (Fig. 3g). This reduction indicates that the STA/PAAm coating not only suppresses the HER but also effectively inhibits Zn electrode corrosion, enhancing its electrochemical stability and performance.

The Zn^{2+} transference number ($t_{Zn^{2+}}$) was determined using the chronoamperometry method under a constant overpotential of −150 mV to assess the influence of the STA/PAAm coating on the ion migration process (Fig. 3h and S16†).[49] The uncoated Zn electrode exhibited extended two-dimensional (2D) diffusion compared to STA/PAAm@Zn. This prolonged 2D diffusion of Zn^{2+} resulted in uneven nucleation, leading to irregular Zn dendrite growth.[50] Conversely, the STA/PAAm coating created a well-organized, ionophilic surface that minimized the 2D diffusion of Zn^{2+} on the electrode surface, facilitated uniform Zn^{2+} deposition, and mitigated irregular dendrite formation. The Zn^{2+} transference number ($t_{Zn^{2+}}$) in the symmetric zinc battery was calculated using the Bruce–Vincent eqn (1):[51]

$$t_{Zn^{2+}} = \frac{I_S(\Delta V - I_0 R_0)}{I_0(\Delta V - I_S R_S)} \tag{1}$$

Here, ΔV represents the applied voltage polarization, while I_S and R_S denote the steady-state current and resistance, and I_0 and R_0 correspond to the initial current and resistance.

The $t_{Zn^{2+}}$ for the STA/PAAm@Zn symmetric battery is 0.48, reflecting an improvement of 0.25 compared to the bare Zn symmetric battery (0.23). This enhancement is attributed to the STA/PAAm coating's capacity to effectively alter the solvation structure of $[Zn(H_2O)_6]^{2+}$. Hydrated Zn^{2+} ions are surrounded by water molecules, and the intact solvation structure introduces resistance during ion transport. Functional groups present in the STA/PAAm coating interact with Zn^{2+}, partially substituting water molecules and disrupting the solvation layer. This modification facilitates faster desolvation of Zn^{2+} ions, thereby lowering the energy barrier for ion diffusion. The activation energy (E_a) is determined using the Arrhenius eqn (2):[52]

$$\frac{1}{R_{ct}} = A \exp\left(-\frac{E_a}{RT}\right) \tag{2}$$

In this equation, R_{ct} represents the charge transfer resistance, A is the frequency factor, R denotes the gas constant, and T is the absolute temperature.

The activation energy (E_a) derived from the Arrhenius equation is 20.19 kJ mol^{-1} for the STA/PAAm@Zn electrode, compared to 26.85 kJ mol^{-1} for the bare Zn electrode (Fig. 3i and S17†). These findings indicate that the STA/PAAm coating may enhance Zn^{2+} ion transfer by modifying the solvation structure of Zn^{2+} and improving the ion conduction properties of the electrode surface.[53]

To evaluate coulombic efficiency (CE) during Zn^{2+} plating/stripping, Zn//bare Cu and Zn//STA/PAAm@Cu asymmetric cells were assembled by pairing bare Cu and STA/PAAm@Cu electrodes with Zn electrodes (Fig. 3j and S18†). At 2 mA cm^{-2}

with a capacity of 1 mA h cm^{-2}, the Zn//STA/PAAm@Cu cell achieved an average CE of 99.93% over 2000 cycles, whereas the Zn//bare Cu cell displayed severe CE fluctuations after about 456 cycles, eventually failing. At 4 mA cm^{-2} with a capacity of 2 mA h cm^{-2}, the Zn//STA/PAAm@Cu cell exhibited notable stability, with the CE remaining at 99.61% after 500 cycles (Fig. S19†). Compared to STA/PAAm-coated Zn electrodes, Zn deposition on bare Cu is highly uneven, leading to the accumulation of "dead Zn" and irreversible capacity loss. As a result, the coulombic efficiency (CE) of the Zn//bare Cu cell fluctuates significantly, dropping to 82.37% by the 217th cycle (Fig. S20†). The bare Cu electrode lacks an effective structure to guide Zn^{2+} deposition, resulting in non-uniform deposition and eventual cell failure.

Through MD simulations, the solvation structure of the STA/PAAm hydrogel membrane was investigated. The results indicate that in the 2 M $Zn(OTf)_2$ electrolyte solution, the predominant solvation form of Zn^{2+} is $[Zn(H_2O)_6]^{2+}$ (Fig. 4a). In this environment, a Zn–O peak is observed at about 2 Å, reflecting the coordination of water molecules with Zn^{2+} and an average coordination number (ACN) of 5.21 (Fig. 4b). In contrast, a 3D simulation snapshot of the STA/PAAm hydrogel membrane reveals that STA and AAm molecules can penetrate the solvation shell of Zn^{2+}, resulting in the formation of a $[Zn(H_2O)_4(STA)(AAm)]^{2+}$ structure alongside water molecules (Fig. 4c). In the hydrogel membrane model, the Zn–O peak similarly appears around 2 Å, which corresponds to interactions among H_2O, STA, and AAm molecules within the solvation shell. The coordination numbers (ACNs) for Zn–H_2O, Zn-STA, and Zn-AAm are 4.86, 0.93, and 0.98, respectively, indicating that STA and AAm molecules contribute significantly to the solvation environment of Zn^{2+}.

To further validate the coordination environment changes predicted by simulations, Raman and nuclear magnetic

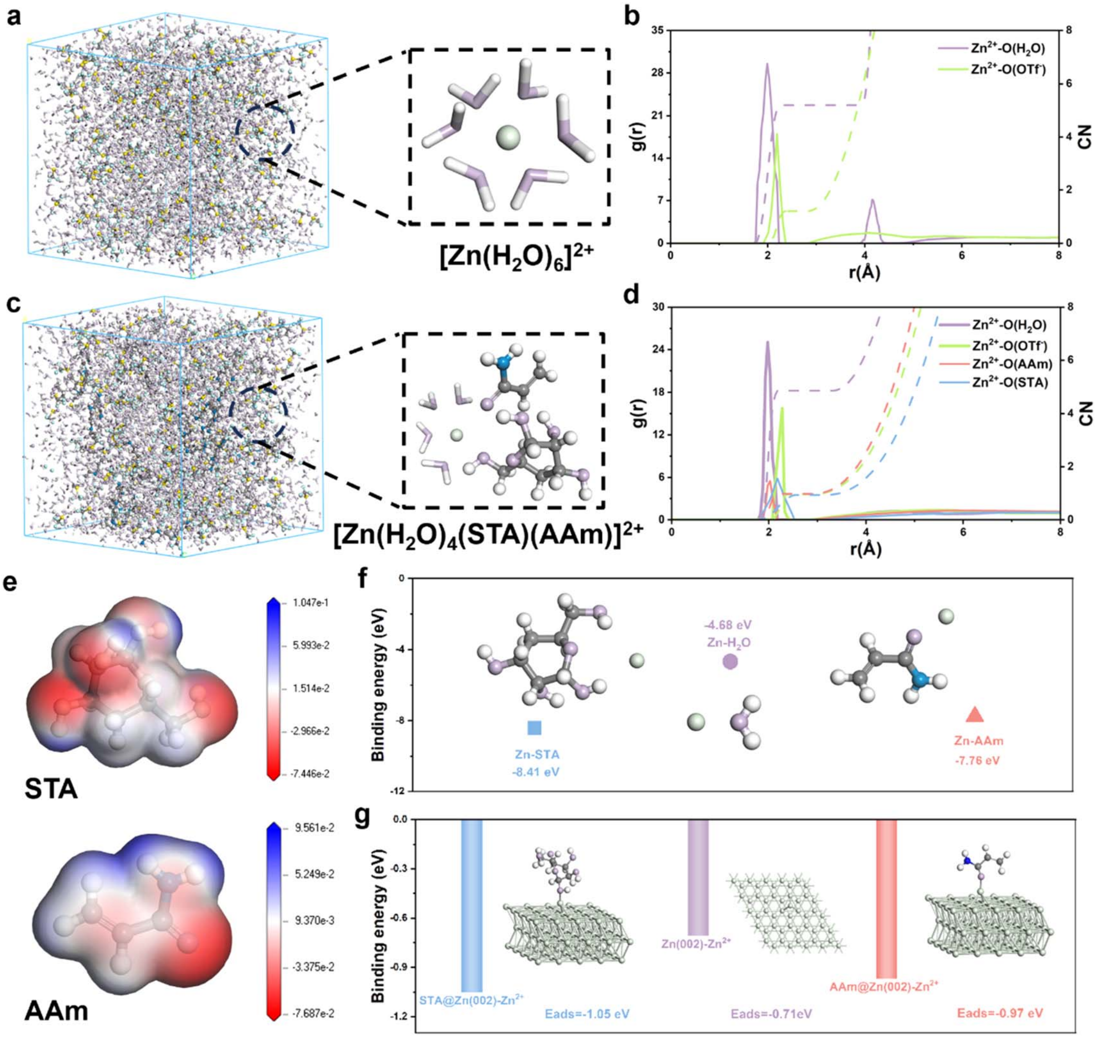

Fig. 4 (a) MD simulation snapshot and typical solvation structure of Zn^{2+} in the $Zn(OTf)_2$ solution. (b) RDF of Zn^{2+}–H_2O and Zn^{2+}-OTf pairs in the $Zn(OTf)_2$ solution obtained from MD simulation, along with the corresponding coordination number. (c) MD simulation snapshot and typical solvation structure of Zn^{2+} in the STA/PAAm hydrogel film. (d) RDF of Zn^{2+}–H_2O, Zn^{2+}-OTf, Zn^{2+}-AAm, and Zn^{2+}-STA pairs in the STA/PAAm film obtained from MD simulation, along with the corresponding coordination number. (e) Electrostatic potential distribution of STA and AAm. (f) Binding energies of Zn–H_2O, Zn-AAm, and Zn-STA. (g) Binding energies of Zn(002)-Zn^{2+}, AAm@Zn(002)-Zn^{2+}, and STA@Zn(002)-Zn^{2+}.

resonance (NMR) analyses were conducted on both the STA/PAAm hydrogel and 2 M $Zn(OTf)_2$ electrolyte systems. Raman results revealed a blue shift of the characteristic peak of the $–SO_3^-$ group in OTf^- (1033 cm^{-1}) in the STA/PAAm compared to the pure electrolyte, indicating the formation of new coordination interactions between Zn^{2+} and STA/PAAm molecules, and a reconstruction of the solvation environment (Fig. S21†).[54] ^1H NMR results showed a downfield shift in the water proton resonance signal in the hydrogel system relative to the pure 2 M $Zn(OTf)_2$ solution. This suggests that the –OH and C=O functional groups in STA and AAm form hydrogen bonds with water molecules, weakening the intrinsic $H_2O–H_2O$ hydrogen-bond network and thus modulating the solvation shell of Zn^{2+}. In addition, ^{67}Zn NMR revealed an upfield shift of the Zn^{2+} resonance peak in the STA/PAAm hydrogel compared to the pure electrolyte, indicating that some of the water molecules in the solvation shell were replaced by coordinating groups from STA and AAm (Fig. S22†).[55] The observed signal broadening further confirms the formation of a more complex and static coordination structure. These experimental findings are in excellent agreement with the MD simulations, which predicted the penetration of STA and AAm into the primary solvation shell of Zn^{2+}.

Electrostatic potential analysis of STA and AAm molecules demonstrates that the oxygen-containing functional groups in both exhibit strong negative charges, enabling the STA/PAAm hydrogel membrane to efficiently capture Zn^{2+} and accelerate its desolvation process (Fig. 4e).[56] Furthermore, STA and AAm molecules act as active sites that facilitate the "hopping" transport mechanism of Zn^{2+} between these groups, promoting rapid and uniform ion migration.[57] DFT calculations indicate that the binding energies of Zn^{2+} with STA and AAm are higher than those with water molecules, suggesting that Zn^{2+} preferentially coordinates with STA and AAm to form a stable coordination structure, thereby modulating its solvation shell (Fig. 4f). This modulation enables Zn^{2+} to deposit evenly on the electrode surface, avoiding local concentration imbalances and mitigating the risk of dendrite formation.[58] At the STA@Zn (002) interface, the binding energy of Zn^{2+} is −1.05 eV, at the AAm@Zn (002) interface it is −0.97 eV, while at the bare Zn (002) interface it is only −0.71 eV (Fig. 4g). These findings confirm that the STA/PAAm@Zn (002) interface exhibits a significantly higher affinity for Zn^{2+}, fostering uniform deposition along the (002) plane and effectively inhibiting dendrite growth.[59]

The Zn^{2+} plating process on STA/PAAm@Zn and bare Zn electrodes was examined using optical microscopy at a current density of 8 mA cm^{-2} and a capacity of 4 mA h cm^{-2} to assess the STA/PAAm hydrogel membrane's effectiveness in suppressing Zn dendrite formation and the HER. During Zn^{2+} deposition, the bare Zn electrode showed numerous Zn dendrite clusters and H_2 bubbles, indicative of an uneven plating process and HER as a side reaction (Fig. 5a). In contrast, the STA/PAAm SEI-coated Zn electrode effectively suppressed dendrite growth and HER, maintaining a flat and dendrite-free Zn deposition layer (Fig. 5b). To evaluate the impact of STA/PAAm as an SEI on Zn plating/stripping stability, symmetric cells with bare Zn//bare Zn and STA/PAAm@Zn//STA/PAAm@Zn configurations were tested. The STA/PAAm@Zn//STA/PAAm@Zn cell demonstrated a cycling lifetime exceeding 3000 h at 2 mA cm^{-2} with a capacity of 1 mA h cm^{-2}, significantly outperforming the bare Zn//bare Zn cell, which lasted only 531 h (Fig. 5c and S23†). At 4 mA cm^{-2} with a capacity of 2 mA h cm^{-2}, the STA/PAAm@Zn//STA/PAAm@Zn symmetric batteries can maintain stability for 1000 h, while the bare Zn//bare Zn cell short-circuited after 119 h (Fig. 5d and S24†). To comprehensively evaluate the performance advantages of the STA/PAAm hydrogel, we systematically compared it with various representative interfacial engineering strategies reported in recent years, including MOFs, MXenes, CNTs, metal coatings, as well as dual-network hydrogel electrolytes (Tables S3 and S4†). Although traditional inorganic SEI coatings have demonstrated certain improvements in Zn anode stability—typically achieving stable cycling of around 200–1500 hours at current densities of 0.2–2 mA cm^{-2}—their synthesis usually involves high-temperature processing, strong corrosive acids, or organic solvents, resulting in high energy consumption and significant environmental burden. Dual-network hydrogel electrolytes reported in the literature may achieve stable cycling over 300–3000 hours under low current densities (0.25–0.5 mA cm^{-2}), but their durability drops significantly at higher current densities (1 mA cm^{-2}). The STA/PAAm hydrogel, although exhibiting lower ionic conductivity and mechanical strength compared to conventional hydrogel electrolytes, demonstrates outstanding performance as a naturally derived and environmentally friendly SEI layer. Its intrinsic self-healing capability imparts superior dynamic adaptability and interfacial compatibility, enabling over 3000 hours of stable cycling at 2 mA cm^{-2}. This exceptional cycling stability clearly surpasses that of most traditional SEI coatings and dual-network hydrogel electrolytes (Fig. 5e and S25†). Its biodegradability and sustainable origin make it a highly promising candidate for application in high-performance AZBs.

SEM images of the STA/PAAm@Zn electrode and the bare Zn electrode after cycling revealed pronounced structural differences (Fig. S26†). The bare Zn anode exhibited numerous flaky byproducts and loose clusters of Zn dendrites. These dendritic structures, characterized by their sharp and irregular morphology, pose a risk of piercing the battery separator during growth, potentially causing internal short-circuiting (Fig. S26a and S27a†). Conversely, the STA/PAAm@Zn surface displayed relatively smooth Zn deposition, effectively preventing dendrite penetration into the diaphragm and enhancing the cycle stability of the battery (Fig. S26b and S27b†). Cross-sectional SEM and EDS images reveal that, in the absence of a surface protective layer, Zn deposition is highly irregular with prominent dendritic protrusions (Fig. S28†). In contrast, for STA/PAAm@Zn, Zn^{2+} deposition occurs beneath the hydrogel layer, forming a dense and uniform structure (Fig. S29†). The spatial distribution of key elements within the SEI layer was examined using time-of-flight secondary ion mass spectrometry (ToF-SIMS) on the cycled STA/PAAm@Zn electrode, focusing on the surface and near-surface region (∼1 μm depth) (Fig. S30†). Uniform distributions of C, O, and Al were observed throughout

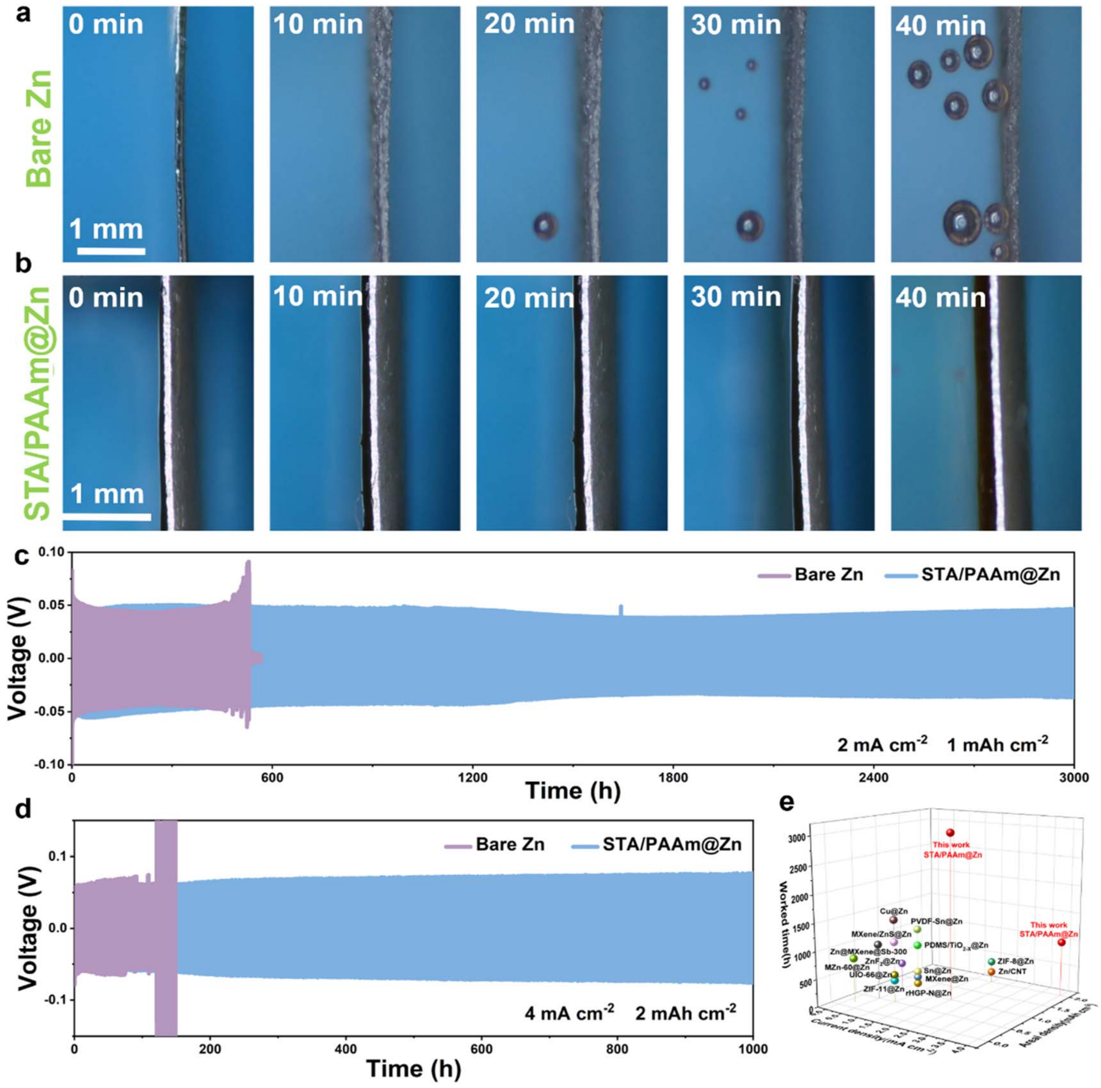

Fig. 5 *In situ* optical microscopy images of (a) bare Zn and (b) STA/PAAm@Zn captured at a current density of 8 mA cm^{-2}. (c) Long-term cycling stability of bare Zn and STA/PAAm@Zn symmetrical batteries at 2 mA cm^{-2} with a capacity of 1 mA h cm^{-2}. (d) Long-term cycling stability of bare Zn and STA/PAAm@Zn symmetrical batteries at 4 mA cm^{-2} with a capacity of 2 mA h cm^{-2}. (e) Comparison of cycle life of STA/PAAm@Zn electrodes with reported Zn anodes featuring various SEI coatings.

the scanned depth, indicating excellent compositional homogeneity and structural integrity of the STA/PAAm hydrogel's double-network structure. Notably, Zn signals showed slight surface enrichment but remained relatively uniform across the hydrogel interior. This pattern suggests effective interfacial coordination of Zn^{2+} and sustained ion transport pathways within the SEI layer. Such a distribution implies that the STA/PAAm hydrogel not only promotes initial Zn^{2+} adsorption at the interface but also supports homogeneous Zn^{2+} migration throughout the SEI—a key factor for dendrite-free deposition and long-term cycling stability.

To further investigate the suppression of HER, we compared the thickness changes of bare Zn symmetric cells and STA/PAAm@Zn symmetric cells before and after cycling (Fig. S31†). The bare Zn symmetric cell exhibited a significant thickness increase from the initial 2.91 mm to 4.15 mm after 100 cycles, accompanied by noticeable bulging. In contrast, the STA/PAAm@Zn symmetric cell showed almost no thickness change after cycling, confirming its effective inhibition of HER. X-ray diffraction (XRD) analysis indicated that the I(002)/I(101) ratio for STA/PAAm@Zn after cycling was 1.26, significantly higher than the value for bare Zn (0.31) (Fig. S32†). This finding confirms that the STA/PAAm coating promotes uniform Zn^{2+} deposition along the Zn (002) plane.[60] Furthermore, XRD signals associated with byproduct $Zn_x(OTf)_y(OH)_{2x-y}\cdot nH_2O$ were prominently observed on the bare Zn surface but were nearly absent on the STA/PAAm@Zn surface. These results suggest that the STA/PAAm coating effectively suppresses the HER side reaction and minimizes electrolyte-induced corrosion on the electrode surface.

The charge transfer resistance (R_{ct}) values derived from electrochemical impedance spectroscopy (EIS) fitting provide insight into the efficiency of charge transfer at the electrode–electrolyte interface (Fig. S33†). The bare Zn symmetric cell exhibited the highest initial R_{ct}, which increased significantly after cycling, indicating progressive degradation of the interfacial structure and inhibited charge transfer. This substantial increase in R_{ct} is primarily attributed to interface instability caused by Zn dendrite growth and side reactions. In contrast, the STA/PAAm@Zn electrode displayed a much lower initial R_{ct}, reflecting enhanced charge transfer efficiency at the interface in its initial state. This reduced R_{ct} is attributed to the STA/PAAm coating's ability to establish a uniform ion transport channel and a stable interfacial environment, effectively lowering diffusion and transfer resistance at the interface. Furthermore, the increase in R_{ct} after cycling was notably smaller for the STA/PAAm@Zn electrode compared to the bare Zn electrode, indicating that the STA/PAAm coating preserves the stability of the interfacial structure over extended charge/discharge cycles. This stability mitigates Zn dendrite growth and side reactions, contributing to improved cycling performance and durability.

To demonstrate the practicality of the Zn anode, a full cell was assembled using STA/PAAm@Zn as the anode and an AlVO-NMP cathode, prepared based on established methods. Cyclic voltammetry (CV) curves indicated that both STA/PAAm@Zn//AlVO-NMP and bare Zn//AlVO-NMP cells exhibited characteristic redox peaks, corresponding to the embedding and deembedding processes of Zn^{2+} and H^+ ions in the AlVO-NMP electrode (Fig. 6a). The STA/PAAm@Zn//AlVO-NMP cell exhibited superior rate performance, delivering higher specific capacities across various current densities compared to the bare Zn//AlVO-NMP cell (Fig. 6b and S34†). At a current density of 0.2 A g^{-1}, the STA/PAAm@Zn//AlVO-NMP full cell achieved a discharge specific capacity of 400.4 mA h g^{-1}, outperforming the bare Zn//AlVO-NMP cell's 363.3 mA h g^{-1} (Fig. 6c). This improvement is attributed to the STA/PAAm coating's formation of a stable interfacial layer, which reduces side reactions and the charge transfer resistance (R_{ct}) at the electrode/electrolyte interface (Fig. 6d).

In long-term cycling tests, the STA/PAAm@Zn//AlVO-NMP battery demonstrated outstanding electrochemical stability. After 500 cycles at 0.2 A g^{-1}, it retained a stable discharge capacity of 324.7 mA h g^{-1}, corresponding to a capacity retention of 83.9% (Fig. S35†), which is significantly higher than that of the bare Zn//AlVO-NMP battery (Fig. S36†). Under the low current density, the relatively slow ion diffusion prolongs the contact time between the cathode and electrolyte, which can induce slight dissolution of the AlVO-NMP active material and lead to capacity decay. Corresponding SEM images (Fig. S37†) show that the AlVO-NMP electrode surface developed cracks and underwent slight structural collapse after cycling at 0.2 A g^{-1}. In contrast, at a high current density of 5 A g^{-1}, the rapid charge/discharge process significantly shortens the interaction time between the electrode and electrolyte, effectively suppressing cathode dissolution and enhancing cycling stability (Fig. S38†). Under this condition, the STA/PAAm@Zn//AlVO-NMP battery initially delivered a discharge specific capacity of 228.2 mA h g^{-1} at 5 A g^{-1}. After 2000 cycles, the specific capacity remained at 198.9 mA h g^{-1}, corresponding to a capacity retention of 87.2%. In contrast, the bare Zn//AlVO-NMP battery exhibited rapid capacity decay at 5 A g^{-1}, with a capacity retention of only 59.1% after 2000 cycles (Fig. 6e and S39†). Further SEM characterization revealed that after 100 cycles at 5 A g^{-1}, the bare Zn electrode surface developed rough dendrites and uneven deposition, whereas the STA/PAAm@Zn electrode maintained a dense and uniform morphology, further confirming the crucial role of the STA/PAAm hydrogel in regulating interfacial morphology and enhancing long-term cycling performance (Fig. S40†).

To evaluate the practical flexibility and application potential of the STA/PAAm@Zn//AlVO-NMP device, we fabricated a flexible pouch cell by electroplating Zn onto carbon cloth as a flexible current collector, followed by the application of a STA/PAAm hydrogel layer as an SEI protective coating. For comparison, a control device using bare Zn without the STA/PAAm coating was prepared under identical conditions. The electrochemical performance of both devices was systematically assessed under initial, curled and folded states. The STA/PAAm@Zn//AlVO-NMP flexible pouch cell exhibited highly stable and reproducible CV and GCD curves under all deformation conditions, indicating excellent mechanical adaptability (Fig. S41 and S42†). In contrast, the bare Zn-based pouch cell showed significantly distorted CV curves and reduced peak currents upon curling and folding. The corresponding GCD curves exhibited shortened discharge plateaus and a rapid voltage drop, along with severe capacity fading, which can be attributed to increased internal resistance and unstable Zn plating/stripping behavior. Additionally, long-term GCD cycling tests were conducted at a current density of 1 A g^{-1} under various bending angles (0°, 45°, 90°, and 180°). The STA/PAAm@Zn//AlVO-NMP cell maintained stable specific capacity with only slight capacity decay across all bending states (Fig. S43†), fully demonstrating the superior mechanical flexibility and interfacial stability endowed by the STA/PAAm hydrogel layer to the Zn anode. In comparison, the bare Zn//AlVO-NMP flexible cell showed significantly poorer capacity retention, with rapid capacity decline as bending severity increased, further confirming the critical role of the hydrogel protective layer in enhancing the mechanical strain tolerance of flexible batteries.[61,62]

Further characterization using a precision resistance tester showed that the STA/PAAm@Zn//AlVO-NMP pouch cells achieved a stable open-circuit voltage (OCV) of 1.575 V, significantly higher than the 1.346 V of bare Zn//AlVO-NMP counterparts, alongside a notable reduction in internal resistance (Fig. 6f and g). Long-term cycling tests at 2 A g^{-1} demonstrated that the STA/PAAm@Zn//AlVO-NMP soft pack full batteries retained 93.4% of their initial capacity after 1500 cycles, outperforming the bare Zn-based devices (78.5% retention), further confirming the critical role of the STA/PAAm hydrogel coating in enhancing electrochemical performance and mitigating capacity decay (Fig. 6h and S44†).

In a practical demonstration, the STA/PAAm@Zn//AlVO-NMP device consistently powered a miniature LED panel under flat, curled and folded states, whereas the bare Zn-based device failed to sustain illumination upon mechanical

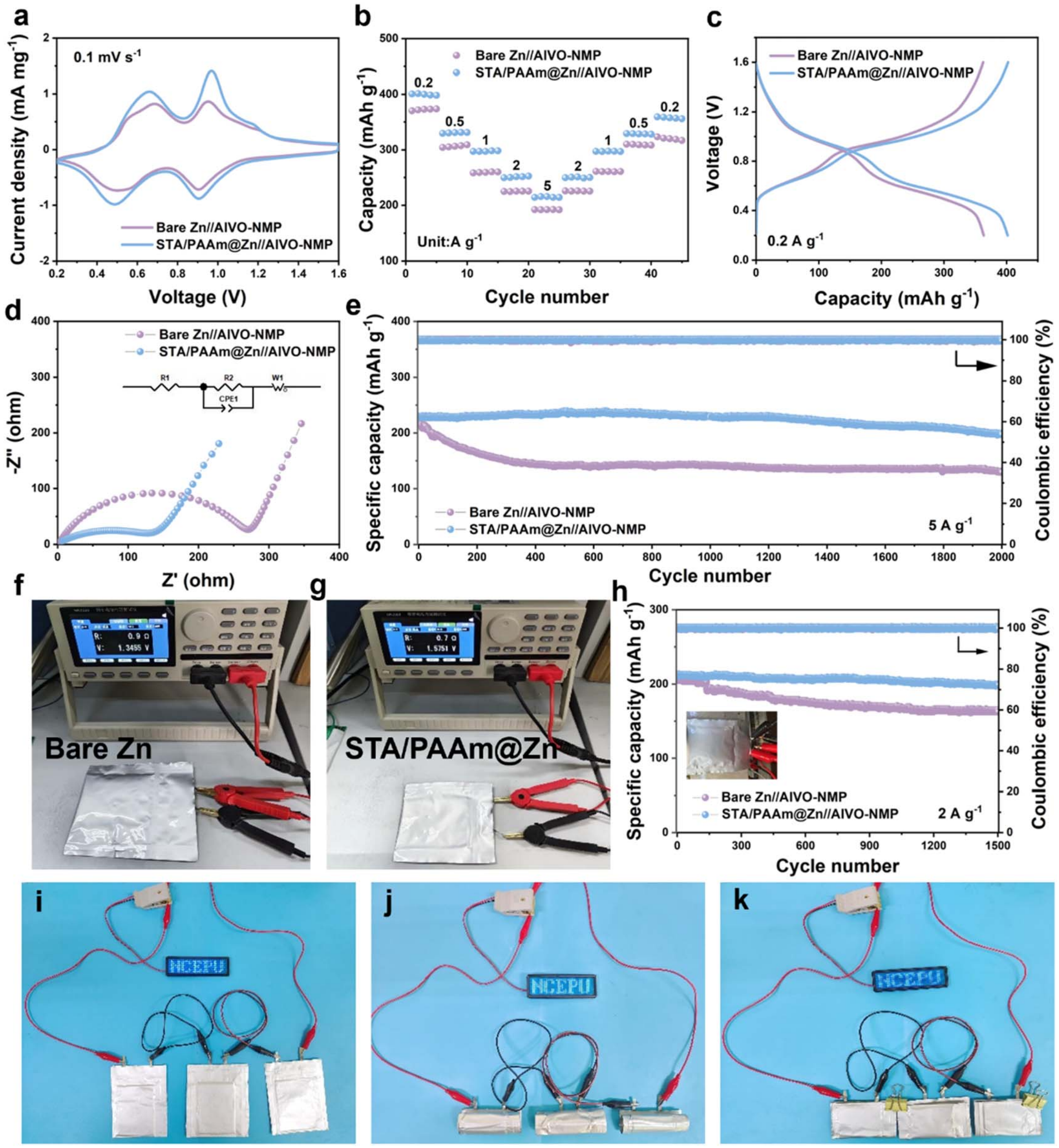

Fig. 6 (a) CV curves. (b) Rate performances. (c) Galvanostatic charge/discharge curves at 0.2 A g^{-1}. (d) Nyquist plots. (e) Cycling behavior of bare Zn//AlVO-NMP and STA/PAAm@Zn//AlVO-NMP coin cells evaluated at a current density of 5 A g^{-1}. The OCVs and internal resistances of (f) bare Zn//AlVO-NMP and (g) STA/PAAm@Zn//AlVO-NMP pouch batteries were measured. (h) Long-term cycling performance of pouch-type bare Zn//AlVO-NMP and STA/PAAm@Zn//AlVO-NMP batteries evaluated at a current density of 2 A g^{-1}. STA/PAAm@Zn//AlVO-NMP soft pack batteries light LED panels in the (i) initial, (j) curled and (k) folded states.

deformation (Fig. 6i–k and S45†). These results collectively highlight the dual advantages of the STA/PAAm hydrogel: it not only significantly extends cycling stability but also provides a robust foundation for constructing mechanically durable and electrochemically reliable flexible aqueous zinc-ion batteries, demonstrating promising practicality and application potential.

Conclusions

This study presents a multifunctional, biomass-derived STA/PAAm dual-network hydrogel membrane as a high-performance solid–electrolyte interphase (SEI) coating for zinc anodes in aqueous batteries. The introduction of dynamic Al^{3+}-mediated crosslinking not only imparts robust mechanical integrity and flexibility but also endows the hydrogel with reliable self-healing capabilities. Molecular dynamics (MD) simulations demonstrate that the STA/PAAm hydrogel effectively modulates the Zn^{2+} solvation structure, forming a $[Zn(H_2O)_4(STA)(AAm)]^{2+}$ configuration that accelerates desolvation and provides active sites for efficient Zn^{2+} migration. Density functional theory (DFT) calculations confirm the strong affinity of STA/PAAm@Zn for Zn^{2+}, facilitating uniform Zn^{2+} deposition on the anode surface and mitigating dendrite formation.

Electrochemical evaluations demonstrate that the STA/PAAm@Zn electrode achieves an extended lifespan exceeding 3000 hours under 2 mA cm^{-2} and 1 mA h cm^{-2}. Moreover, the STA/PAAm@Zn//AlVO-NMP soft-pack full cell delivers a high specific capacity of 228.2 mA h g^{-1} at 5 A g^{-1}, while retaining 87.2% of its initial capacity after 2000 cycles. Beyond electrochemical performance, the hydrogel coating also exhibits excellent biodegradability in soil, addressing growing environmental concerns associated with non-degradable SEI materials. This study offers a promising strategy for designing eco-friendly and functional hydrogel-based composite interfaces for advanced zinc-ion batteries, synergizing high-performance energy storage with environmental sustainability.

Data availability

The data supporting this article have been included as part of the ESI.†

Author contributions

Zinan Wang: conceptualization, methodology, software, writing – original draft. Tianxu Ji: methodology, software, visualization. Qilin Zhang: investigation, software. Peng Wang: funding acquisition, project administration, resources, writing – review and editing. Xiaoyu Yang: methodology, software. Shuo Zhang: methodology, validation. Yuhang Jin: validation. Jiaxuan Zhang: validation. Wei Duan: project administration, supervision, validation. Ying Yue: project administration, supervision, validation. Yang Ju: formal analysis, resources. Yunpeng Liu: formal analysis, resources.

Conflicts of interest

The authors declare that they have no conflict of interest.

Acknowledgements

This work was supported by Distinguished Young Scholars of Hebei Province (E2024502077), Beijing Natural Science Foundation (3232054), National Nature Science Foundation of China (51977079), Key Laboratory of Icing and Anti/De-icing of CARDC (Grant No. IADL 20210401), the Central Guidance on Local Science and Technology Development Fund of Hebei Province (226Z1204G), Basic Research Project of Baoding City (2272P002), the Top Young Innovative Talents of Colleges and universities of Higher Learning Institutions of Hebei (BJ2021095), the Fundamental Research Funds for the Central Universities (2025MS139) and Smart Grid-National Science and Technology Major Project (2024ZD0803100).

References

1 A. M. Aghdam, N. M. Chahartagh, S. Namvar, M. Ershadi, F. B. Ajdari and E. Delfani, *J. Mater. Chem. A*, 2024, **12**, 1047–1057.
2 P. Guo, G. Yang and C. Wang, *J. Mater. Chem. A*, 2021, **9**, 16868–16877.
3 H. B. Jeong, D. I. Kim, G. Yoo, D. Mohan, A. Roy, M. Jung, H. S. Jeong, S. Cha, G.-H. An and P.-R. Cha, *J. Mater. Chem. A*, 2024, **12**, 15265–15277.
4 Z. Wang, X. Liu, H. Chen, X. Zhu, L. Song, Y. Yang, J. Bai, M. J. Kim, W. M. Lau and F. Rosei, *J. Mater. Chem. A*, 2023, **11**, 1380–1393.
5 C. Yang, P. Woottapanit, J. Cao, Y. Yue, D. Zhang, J. Yi, Z. Zeng, X. Zhang, J. Qin and Y. Wang, *J. Mater. Chem. A*, 2023, **11**, 24902–24910.
6 Y. Wang, X. Wang, J. Tang and W. Tang, *J. Mater. Chem. A*, 2022, **10**, 13868–13875.
7 Y. Li, S. Yang, H. Du, Y. Liu, X. Wu, C. Yin, D. Wang, X. Wu, Z. He and X. Wu, *J. Mater. Chem. A*, 2022, **10**, 14399–14410.
8 Z. Dong, C. Zhong, H. Chai, G. Weng, J. Chen, X. Guo, Y. Wang, J. Jiang, X. Huang, J. Fan, C. Wei, C. Wu, H. Liu, S. Dou and X. Yang, *Adv. Funct. Mater.*, 2025, 2503502.
9 R. Sun, D. Luo, H. Zhou, Z. Zhang, Y. Gao, S. Ma, Z. Li and X. Kang, *J. Energy Chem.*, 2025, **103**, 703–713.
10 T. Wang, Y. Tang, M. Yu, B. Lu, X. Zhang and J. Zhou, *Adv. Funct. Mater.*, 2023, **33**, 2306101.
11 L. Yan, Y. Han, C. Zhu, L. Luo, Y. Qin, D. Yu, B. Liu, X. Zou, Y. Zhou and B. Xiang, *Nano Energy*, 2024, **122**, 109331.
12 J. Yang, B. Yin, Y. Sun, H. Pan, W. Sun, B. Jia, S. Zhang and T. Ma, *Nano-Micro Lett.*, 2022, **14**, 1–47.
13 Y. Zou, C. Qiao, Y. Su, M. Lu, X. Yang, S. Dou and J. Sun, *Appl. Phys. Lett.*, 2023, **123**, 223903.
14 M. Cui, B. Yan, F. Mo, X. Wang, Y. Huang, J. Fan, C. Zhi and H. Li, *Chem. Eng. J.*, 2022, **434**, 134688.
15 C. Liu, Y. Wang, H. Liu, Q. Chen, X. Jiang, H. Jia and J. Lang, *Composites, Part B*, 2024, **272**, 111227.
16 R. Yuksel, O. Buyukcakir, W. K. Seong and R. S. Ruoff, *Adv. Energy Mater.*, 2020, **10**, 1904215.
17 M. Liu, L. Yang, H. Liu, A. Amine, Q. Zhao, Y. Song, J. Yang, K. Wang and F. Pan, *ACS Appl. Mater. Interfaces*, 2019, **11**, 32046–32051.
18 Y. Zeng, X. Zhang, R. Qin, X. Liu, P. Fang, D. Zheng, Y. Tong and X. Lu, *Adv. Mater.*, 2019, **31**, 1903675.
19 J. Wang, J. Peng, W. Huang, H. Liang, Y. Hao, J. Li, H. Chu, H. Wei, Y. Zhang and J. Liu, *Adv. Funct. Mater.*, 2024, **34**, 2316083.
20 Y. Tian, Y. An, C. Wei, B. Xi, S. Xiong, J. Feng and Y. Qian, *ACS Nano*, 2019, **13**, 11676–11685.
21 Y. Tian, Y. An, C. Liu, S. Xiong, J. Feng and Y. Qian, *Energy Storage Mater.*, 2021, **41**, 343–353.
22 S. Nayak, L. C. Goveas, R. Selvaraj, R. Vinayagam and S. Manickam, *Bioresour. Technol.*, 2022, **364**, 128073.
23 R. Velmurugan, A. K. Chandel and A. Incharoensakdi, *Bioresour. Technol.*, 2024, **398**, 130516.
24 L. Mao, G. Li, B. Zhang, K. Wen, C. Wang, Q. Cai, X. Zhao, Z. Guo and S. Zhang, *Adv. Mater.*, 2024, 2416345.
25 R. Jia, C. Wei, B. Ma, L. Li, C. Yang, B. Wang, L. Tan and J. Feng, *Adv. Funct. Mater.*, 2025, **35**, 2417498.
26 A. C. Radjendirane, F. M. Sha, S. Ramasamy, R. Rajaram and S. Angaiah, *Energy Technol.*, 2024, **12**, 2401105.

27 H. Tiwari, P. Tripathi, R. K. Sonwani and R. S. Singh, *Bioresour. Technol.*, 2023, **387**, 129614.

28 G. Carnovale, C. Lama, S. Torres, F. Rosa, L. Mantecón, S. J. Horn, K. Skjånes and C. Infante, *Bioresour. Technol.*, 2022, **354**, 127222.

29 J. Cao, P. Wu, Q. Cheng, C. He, Y. Chen and J. Zhou, *ACS Appl. Mater. Interfaces*, 2021, **13**, 24095–24105.

30 S. Hadad, M. Hamrahjoo, E. Dehghani, M. Salami-Kalajahi, S. N. Eliseeva, A. R. Moghaddam and H. Roghani-Mamaqani, *Appl. Energy*, 2022, **324**, 119767.

31 F. Wan, Z. Hao, S. Wang, Y. Ni, J. Zhu, Z. Tie, S. Bi, Z. Niu and J. Chen, *Adv. Mater.*, 2021, **33**, 2102701.

32 Y. Zuo, X. He, P. Li, W. Li and Y. Wu, *Polymers*, 2019, **11**, 72.

33 C. Chen, X. Yang, S. Li, C. Zhang, Y. Ma, Y. Ma, P. Gao, S. Gao and X. Huang, *Green Chem.*, 2021, **23**, 1794–1804.

34 S. Yang, Y. Zhang, T. Wang, W. Sun and Z. Tong, *ACS Appl. Mater. Interfaces*, 2020, **12**, 46701–46709.

35 S. J. Kerber, J. J. Bruckner, K. Wozniak, S. Seal, S. Hardcastle and T. L. Barr, *J. Vac. Sci. Technol., A*, 1996, **14**, 1314–1320.

36 X. Yang, P. Wang, X. Wu, Y. Liao, S. Liu, W. Duan and Y. Yue, *Chin. J. Chem.*, 2024, **42**, 543–556.

37 Y. Chen, L. Liu, Y. Huang, H. Cao, T. Liu, Z. Qi, J. Hu, Y. Guo, J. Sun and M. Liang, *Appl. Energy*, 2024, **363**, 123100.

38 S. Yang, Y. Zhang, T. Wang, W. Sun and Z. Tong, *ACS Appl. Mater. Interfaces*, 2020, **12**, 46701–46709.

39 H. Sheng, J. Zhou, B. Li, Y. He, X. Zhang, J. Liang, J. Zhou, Q. Su, E. Xie and W. Lan, *Sci. Adv.*, 2021, **7**, eabe3097.

40 X. Huang, H. Hou, B. Yu, J. Bai, Y. Guan, L. Wang, K. Chen, X. Wang, P. Sun and Y. Deng, *ACS Nano*, 2023, **17**, 5727–5739.

41 H. Zhang, R. Wang, Z. Chen and Q. Zhong, *J. Agric. Food Chem.*, 2020, **68**, 3796–3805.

42 S. Sun, J. Guo, Z. Zhu and J. Zhou, *Front. Microbiol.*, 2024, **15**, 1500401.

43 T. Krithiga, S. Sathish, A. A. Renita, D. Prabu, S. Lokesh, R. Geetha and S. K. R. Namasivayam, *Sci. Total Environ.*, 2022, **831**, 154808.

44 H. Peng, D. Wang, F. Zhang, L. Yang, X. Jiang, K. Zhang, Z. Qian and J. Yang, *ACS Nano*, 2024, **18**, 21779–21803.

45 H. Zhang, X. Gan, Z. Song and J. Zhou, *Angew. Chem., Int. Ed.*, 2023, **135**, e202217833.

46 W. Fu, M. Guo, X. Zhou, Z. Wang, J. Sun, Y. An, T. Guan, M. Hu, J. Li and Z. Chen, *ACS Nano*, 2024, **18**, 11200–11216.

47 J. Seo, R. Singh, J. Ryu and J. H. Choi, *J. Chem. Inf. Model.*, 2023, **64**, 138–149.

48 Y. Mu, F. Chu, B. Wang, T. Huang, Z. Ding, D. Ma, F. Liu, H. Liu and H. Wang, *InfoMat*, 2024, **6**, e12611.

49 X. Yang, Y. Lu, Z. Liu, H. Ji, Z. Chen, J. Peng, Y. Su, Y. Zou, C. Wu, S. Dou, P. Gao, Z. Guo and J. Sun, *Energy Environ. Sci.*, 2024, **17**, 5563–5575.

50 Y. Zhang, X. Li, L. Fan, Y. Shuai and N. Zhang, *Cell Rep. Phys. Sci.*, 2022, **3**, 100824.

51 E. Xu, L. Mo, Y. Zhou, Z. Cheng, P. Li, X. Tian, W. Yang, C. Lai, P. Dou and Z. Yuan, *Appl. Energy*, 2025, **377**, 124750.

52 Y. Feng, L. Zhou, H. Ma, Z. Wu, Q. Zhao, H. Li, K. Zhang and J. Chen, *Energy Environ. Sci.*, 2022, **15**, 1711–1759.

53 C. Meng, W. He, L. Jiang, Y. Huang, J. Zhang, H. Liu and J. Wang, *Adv. Funct. Mater.*, 2022, **32**, 2207732.

54 H. Tian, M. Yao, Y. Guo, Z. Wang, D. Xu, W. Pan and Q. Zhang, *Adv. Energy Mater.*, 2025, **15**, 2403683.

55 Y. Huang, R. Guo, Z. Li, J. Zhang, W. Liu and F. Kang, *Adv. Sci.*, 2024, **11**, 2407201.

56 W. Lu, Y. Shao, R. Yan, Y. Zhong, J. Ning and Y. Hu, *Batteries Supercaps*, 2024, **7**, e202300486.

57 X. Li, Y. Li, Y. Jiang, D. Wang and F. Ran, *Green Energy Environ.*, 2024, **10**, 537–550.

58 F. Tan, X. Cai, W. Yan, Q. Wang, J. Zhao and W. Zhang, *Energy Storage Mater.*, 2024, **67**, 103273.

59 D. Deng, K. Fu, R. Yu, J. Zhu, H. Cai, X. Zhang, J. Wu, W. Luo and L. Mai, *Adv. Mater.*, 2023, **35**, 2302353.

60 X. Yang, Z. Dong, G. Weng, Y. Su, J. Huang, H. Chai, Y. Zhang, K. Wu, J.-B. Baek, J. Sun, D. Chao, H. Liu, S. Dou and C. Wu, *Adv. Energy Mater.*, 2024, **14**, 2401293.

61 A. C. Radjendirane, S. Ramasamy, S. P. Rajendra, G. Murali, I. In, S. J. Lee and S. Angaiah, *Electrochim. Acta*, 2025, **531**, 146368.

62 A. C. Radjendirane, F. M Sha, B. Balan, S. Ramakrishnan, K. Vediappan, S. P. Rajendra, M. S. Alsalhi and S. Angaiah, *ACS Appl. Energy Mater.*, 2024, **7**, 4745–4760.